

Full length article

Strain hardening by dynamic slip band refinement in a high-Mn lightweight steel



E. Welsch^a, D. Ponge^{a,*}, S.M. Hafez Haghighat^a, S. Sandlöbes^{a,b}, P. Choi^{a,c}, M. Herbig^a, S. Zaefferer^a, D. Raabe^a

^a Max-Planck-Institut für Eisenforschung, Max-Planck-Str. 1, 40237 Düsseldorf, Germany

^b Institute of Physical Metallurgy and Metal Physics, RWTH Aachen University, 52056 Aachen, Germany

^c Korea Advanced Institute of Science and Technology (KAIST), 291 Daehak-ro, Yuseong-gu, Daejeon 305-338, Republic of Korea

ARTICLE INFO

Article history:

Received 24 March 2016

Received in revised form

13 June 2016

Accepted 15 June 2016

Keywords:

ECCI

Strain hardening

Dynamic slip band refinement

High-manganese light weight steel

ABSTRACT

The strain hardening mechanism of a high-Mn lightweight steel (Fe-30.4Mn-8Al-1.2C (wt%)) is investigated by electron channeling contrast imaging (ECCI) and transmission electron microscopy (TEM). The alloy is characterized by a constant high strain hardening rate accompanied by high strength and high ductility (ultimate tensile strength: 900 MPa, elongation to fracture: 68%). Deformation microstructures at different strain levels are studied in order to reveal and quantify the governing structural parameters at micro- and nanometer scales. As the material deforms mainly by planar dislocation slip causing the formation of slip bands, we quantitatively study the evolution of the slip band spacing during straining. The flow stress is calculated from the slip band spacing on the basis of the passing stress. The good agreement between the calculated values and the tensile test data shows dynamic slip band refinement as the main strain hardening mechanism, enabling the excellent mechanical properties. This novel strain hardening mechanism is based on the passing stress acting between co-planar slip bands in contrast to earlier attempts to explain the strain hardening in high-Mn lightweight steels that are based on grain subdivision by microbands. We discuss in detail the formation of the finely distributed slip bands and the gradual reduction of the spacing between them, leading to constantly high strain hardening. TEM investigations of the precipitation state in the as-quenched state show finely dispersed atomically ordered clusters (size < 2 nm). The influence of these zones on planar slip is discussed.

© 2016 Acta Materialia Inc. Published by Elsevier Ltd. All rights reserved.

1. Introduction

High-Mn steels attract much attention due to their outstanding combination of strength and ductility caused by their high strain hardening capacity. Weight reduced variants of these austenitic steels are typically characterized by high manganese content (18–30 wt%) and the addition of aluminum (<12 wt%) and silicon (<3 wt%) along with carbon (0.6–1.8 wt%) [1–9]. As increasing the aluminum content yields a reduction in specific weight by 1.5% per 1 wt% Al [10], high aluminum contents render these alloys “light-weight” [11–18].

A variety of hardening mechanisms are reported in high-Mn steels, namely, transformation-induced plasticity (TRIP) [1], twinning-induced plasticity (TWIP) [1,5,6,19–21] and microband-

induced plasticity (MBIP) [2,22,23]. The activation of the dominant deformation mechanism is mainly determined by the stacking fault energy (SFE). The TRIP effect is found to operate predominantly in low-SFE steels (<20 mJ m⁻²). The deformation behavior of medium-SFE steels (20–40 mJ m⁻²) is characterized by the formation of nanometer thin deformation twins in the deformed microstructure, referred to as TWIP effect. The recently discussed MBIP hardening mechanism, reported in high-SFE alloys (~90 mJ m⁻²), is described by the formation of thin planar shear zones that are confined by a dislocation wall on either side. These features are called microbands [2,23,24]. All the above mentioned hardening mechanisms result in strong refinement of the respective microstructures during straining enabling high strain hardening rates.

The SFE not only has a strong influence on the deformation mechanism, but it also controls the glide mode of the dislocations. A high SFE usually promotes cross-slip of dislocations leading to

* Corresponding author.

E-mail address: d.ponge@mpie.de (D. Ponge).

“wavy glide” in pure fcc metals. However, in concentrated solid solutions with high SFEs planar glide instead of wavy glide is frequently observed [25–27]. The reasons for planar glide in such massively alloyed high-SFE materials have been controversially discussed [28,29]. In the quaternary FeMnAlC system aluminum increases the SFE on the one hand but yet promotes planar dislocation glide on the other hand [1,23]. Many authors attributed this seemingly contradicting finding to the material's tendency to form clusters of short-range order (SRO), which leads to enhanced planar glide due to the glide plane softening phenomenon [2,22,28,30–32]. As the addition of aluminum in these alloys promotes the formation of ordered precipitates (κ -carbides), SRO indeed seems to be a plausible explanation [33]. However, to the authors' best knowledge no studies providing experimental proof for SRO in high-Mn lightweight steels have been published so far. Some works though indicate the presence of SRO in the FeMnAlC system and similar alloy systems by using density functional theory (DFT) simulations [34–36].

The κ -carbide is an $L'1_2$ -ordered phase with the stoichiometric composition $(\text{Fe,Mn})_3\text{AlC}$. However, κ -carbides exist at a broad compositional range [37] and coherency strains have an additional influence on their composition [38]. Depending on the aluminum concentration these ordered precipitates either grow during annealing at temperatures between 550 °C and 700 °C (<10 wt% Al) or even during quenching from solution heat treatment temperature (>10 wt% Al) [33,39–45]. Due to the strong influence of these precipitates on the mechanical properties the precipitation kinetics have been subject of several studies [15,41–43,45].

A detailed quantitative characterization of the underlying kinetics of the substructure evolution in the FeMnAlC system has been performed in the case of Fe-30.5Mn-2.1Al-1.2C [46]. With a SFE of about 63 mJ m^{-2} , this alloy, however, falls in the regime between TWIP and MBIP alloys. Yoo et al. investigated the plastic deformation of Fe-28.2Mn-9.95Al-0.98C (wt%) with a SFE of 120 mJ m^{-2} and Fe-27.8Mn-9.1Al-0.79C (wt%) with a SFE of 85 mJ m^{-2} rendering both alloys pure MBIP steels [2,23]. They attribute the high strain hardening capacity to the formation of Taylor-lattices and microbands during straining. However no quantitative results were presented. Furthermore the formation of microbands have been doubted of causing the observed strain hardening rate in the literature [46].

The present study aims at clarifying the deformation mechanism in such materials using a similar alloy (Fe-30.4Mn-8Al-1.2C), with a SFE of 85 mJ m^{-2} [2,8,47] by means of electron channeling contrast imaging (ECCI) and transmission electron microscopy (TEM). The combination of these two techniques constitutes a powerful method for giving insight into the underlying mechanisms of plastic deformation at different length scales [46,48]. The TEM investigation focuses on the initial precipitation state, whereas the large field of view provided by ECCI provides statistical and quantitative data on the structural evolution of deformation features. High-magnification ECCI was used to provide details on the observed dislocation arrangements on the finer scale. In this study the applied ECCI technique exhibits an advantage over the commonly used TEM imaging in terms of sample dimensions, field of view, preparation artifacts and image forces. As TEM samples have a thickness of about 100 nm, dislocations in the sample can change their position due to image forces originating from the two surfaces of the thin foil or from bending. In contrast, ECCI is applied to bulk samples with only one polished surface. Therefore, deformation microstructures that are characteristic of the actual bulk material are investigated rather than relaxed dislocation structures influenced by stress relaxation. In the case of ECCI the image forces from the surface reach less than 20 nm into the sample, while the depth of observation is of the order of 100 nm [49]. Dislocations

will therefore not rearrange as strongly as in TEM thin foils, which enables investigation of the undistorted dislocation structure of bulk samples.

2. Experimental

The chemical composition of the investigated high-Mn steel was Fe-30.4Mn-8Al-1.2C (wt%) as determined by wet chemical analysis. The material was melted in an induction furnace under Ar atmosphere and cast into a 12 kg ingot of 40 mm thickness. In order to homogenize the material and to remove segregation zones originating from solidification, the cast ingot was reheated to 1200 °C for 30 min and hot rolled in multiple passes to an engineering thickness reduction of 75% at 1100 °C followed by water quenching. Bar-shaped samples ($11 \times 11 \times 60 \text{ mm}^3$) were cut from the hot-rolled ingot and solution treated for 2 h at 1100 °C in Ar atmosphere and subsequently quenched in oil. The annealed material was fully austenitic with an average grain size of about 40 μm . Cylindrical tensile test samples were machined from the bars with gage dimensions of 6 mm diameter and 40 mm length. Tensile tests were carried out at room temperature in a Zwick ZH 100 tensile machine with an initial strain rate of $5 \cdot 10^{-4} \text{ s}^{-1}$. Tensile testing up to fracture and interrupted tensile tests up to true strains of $\epsilon = 0.02, 0.05, 0.14, 0.27$ and 0.34 (equivalent to engineering strains of 2, 5, 15, 30, 42%, respectively) were performed in order to track the evolution of the microstructure during plastic deformation.

The initial precipitation state was investigated in a Phillips CM20 and a JEOL JEM-2200FS TEM operated at 200 kV. TEM samples were prepared by electropolishing using a Struers Tenupol twin-jet device. Discs with a diameter of 3 mm were cut from the undeformed head of a tensile sample and mechanically polished to about 100 μm thickness. Electropolishing was carried out at $-30 \text{ }^\circ\text{C}$ and 10 V using a solution of 30% nitric acid in methanol.

The microstructures of the deformed samples were examined by ECCI in two different FEG-SEMs using a solid-state four-quadrant BSE detector. A Zeiss Crossbeam instrument (XB 1540) was used for investigating the microstructure evolution, whereas high magnification images were obtained with a Zeiss 'Merlin' SEM. Acceleration voltage and working distance were set in both cases to 30 kV and 6 mm, respectively. All ECCI samples were prepared with the surface perpendicular to the tensile axis, i.e. the observation direction was always along the tensile axis. Grain orientations were obtained from electron backscatter diffraction (EBSD) using an EDAX EBSD system. Grain orientations were used for slip trace analysis in conjunction with ECCI. The working distance and the acceleration voltage for the EBSD analysis were set to 15 mm and 15 kV, respectively.

3. Results

3.1. Strain hardening

Fig. 1 shows the true stress-true strain curves along with the strain hardening rate at room temperature for an initial strain rate of $5 \cdot 10^{-4} \text{ s}^{-1}$. The material exhibits extraordinary mechanical properties in terms of a high maximum strength of 1440 MPa at failure, in addition to a high uniform elongation of 0.46 and a yield strength of 550 MPa. After a stress drop at the yield point, the strain hardening rate Θ is characterized by a minimum at about $\epsilon = 0.06$ ($\Theta_{0.06} = 1820 \text{ MPa}$) and a maximum at about $\epsilon = 0.27$ true strain ($\Theta_{0.27} = 2100 \text{ MPa}$). In structural metallic alloys commonly a monotonic decay of strain hardening with ongoing strain is observed [50]. Deviations from this behavior are usually attributed to secondary hardening effects (e.g. TWIP, TRIP or MBIP) [3,46]. Interestingly, the strain hardening rate of the current alloy shows

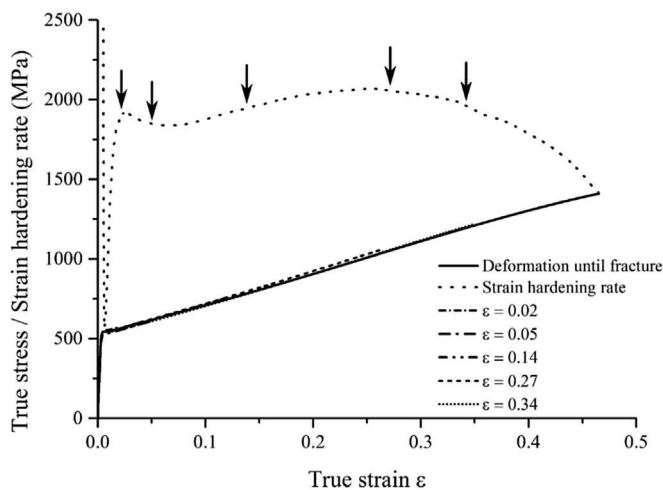


Fig. 1. Set of true stress-true strain curves taken at room temperature of tensile tests performed until failure (solid line) and interrupted tests at $\epsilon = 0.02, 0.05, 0.14, 0.27$ and 0.34 (dashed lines). The strain hardening rate (dotted line) does not show pronounced multistage hardening. The arrows indicate up to which true strains the interrupted tests were strained. The initial strain rate was $5 \cdot 10^{-4} \text{ s}^{-1}$ in all cases.

qualitatively the same strain dependence as observed in TWIP steels as well as in MBIP steels, even though the underlying microstructural mechanisms are entirely different [3,7,23,51]. Pronounced multistage strain hardening, i.e. distinct transitions in the strain hardening rate, pointing at corresponding mechanism changes, such as observed for the alloy Fe-30.5Mn-2.1Al-1.2C [46], is not observed here.

The intersection of the true stress-true strain curve with the strain hardening rate indicates the onset of necking. Fracture after the necking point indicates failure by plastic instability in accordance with Considère's criterion. The active hardening mechanisms can then no longer compensate for the geometrical softening caused by local cross section reduction.

3.2. Precipitation state after quenching

The diffraction pattern of the [001]-zone axis in Fig. 2a exhibits faint (100) superlattice reflections (marked with circles), indicating the occurrence of atomic ordering. These superlattice reflections are attributed to the presence of the ordered κ -carbide phase [41,42,45,52,53]. The growth kinetics of this $L'_{1/2}$ ordered phase is strongly dependent on the aluminum and carbon contents, the

annealing temperature and the cooling rate during quenching [45]. Earlier studies suggested that the formation of κ -carbides occurs via spinodal decomposition [33,45,54].

Fig. 2b shows finely dispersed diffuse atomically ordered clusters (size $< 2 \text{ nm}$) in the as-quenched material by dark-field (DF) TEM using the (100) superlattice reflection. The low intensity of the superlattice reflections indicates a low precipitate volume fraction. However, no quantitative estimate for the volume fraction can be given from this TEM micrograph as the thickness of the thin foil is not exactly known and projection effects prevent a meaningful estimate. The influence of the ordered clusters on the dislocation glide character, dislocation patterning and dislocation banding is discussed in section 3.4.

Since the occurrence of pronounced elemental partitioning, as reported in thermally treated high-Mn lightweight steel [55], is not possible during quenching in the present case, full κ -carbide formation did most probably not occur. Therefore, in the following the observed atomically ordered zones will be referred to as “long-range-ordered clusters” (LRO-clusters). As carbon can diffuse much faster compared to substitutional alloying elements, it is assumed that carbon ordering took place during quenching.

These findings are in good agreement with a previous investigation on the precipitation state of a similar alloy (Fe-30.5Mn-8.0Al-1.2C), where “short annealing” (1 h/450 °C) leads to a random distribution of 2–5 nm large ordered clusters and the presence of weak (100) superlattice reflections in the diffraction pattern [48].

3.3. Evolution of the deformation microstructure

Fig. 3 shows ECCI micrographs of samples which experienced different true tensile strains ($\epsilon = 0.02, 0.05, 0.14, 0.27, 0.34$) illustrating the evolution of the deformation microstructure during straining. All images were taken along the tensile axis, i.e. the image plane is perpendicular to the tensile axis. At a true strain of $\epsilon = 0.02$ (see Fig. 3a,b), the material deforms by planar dislocation glide as commonly observed for fcc alloys at early deformation stages [26,56]. In fcc materials dislocations typically glide on {111} planes, which is also indicated by the slip traces observed in Fig. 3b. The pronounced planar slip behavior leads to the formation of crystallographically aligned slip bands that originate from frequently observed Frank-Read sources, such as indicated by white arrows in Fig. 3 and in the inset in Fig. 3a. Slip bands are defined here as individual crystallographic glide planes with a high dislocation density.

The microstructure at $\epsilon = 0.05$ true strain (Fig. 3c) is also characterized by planar slip bands as already observed at $\epsilon = 0.02$,

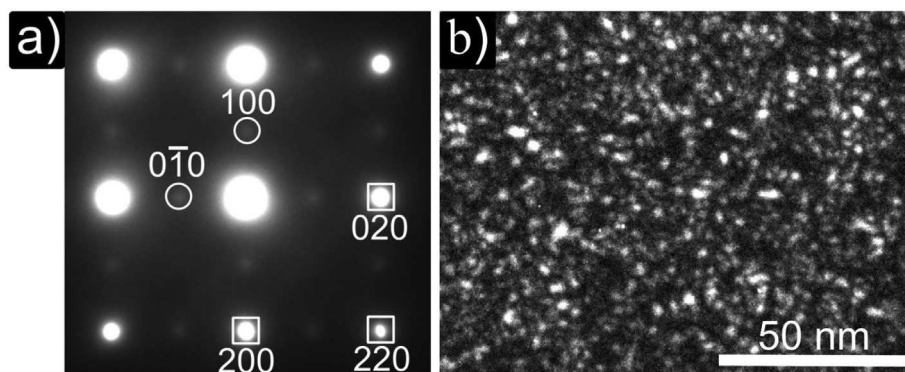


Fig. 2. Diffraction pattern of the [001]-zone axis in the undeformed as-quenched material (a). The presence of weak superlattice reflections (marked with circles) indicates the presence of an atomically ordered structure. Spots labeled with squares belong to the ordered phase as well as to the austenitic matrix. The DF-TEM image in (b) was taken with the (100) superlattice reflection of the ordered clusters. The finely dispersed ordered zones are randomly distributed and exhibit a size of less than 2 nm.

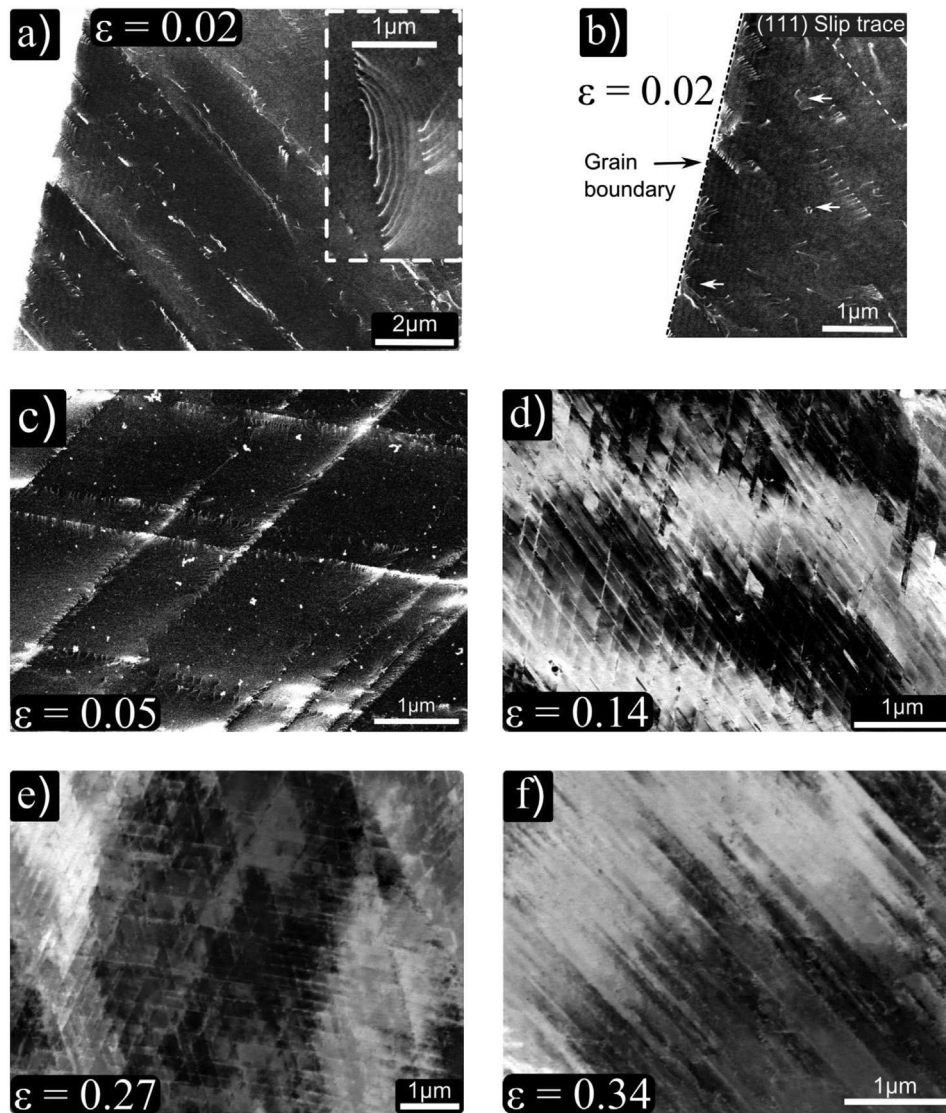


Fig. 3. ECCI micrographs of the deformed microstructures at different true strains ($\epsilon = 0.02$ (a,b), 0.05 (c), 0.14 (d), 0.27 (e), 0.34 (f)). All images were taken along the tensile axis. Pronounced planar slip and the formation of crystallographically aligned slip bands is observed at all true strains. The evolution of the deformation structure is characterized by pronounced gradual refinement of this crystallographic slip band structure during straining and a reduction of the average slip band spacing. In (b) and in the inset in (a) dislocation sources are observed (see arrows) which have emitted dislocations gliding all on the same glide plane. At $\epsilon = 0.02$ gliding dislocations lead to pile-ups at the grain boundary (broken line). Deformation twins are not observed.

however, with a reduced slip band spacing. The slip bands predominantly extend through the entire grains until they impinge the grain boundaries indicating only weak interactions among intersecting slip bands. Obstruction of slip bands by mutual intersection hence does not seem to play a major role at this deformation stage, as slip bands that are limited at intersecting non-coplanar slip bands and corresponding dislocation pile-ups are only rarely observed. At a true strain of $\epsilon = 0.14$ (Fig. 3d) the spacing between co-planar slip bands is further reduced while the overall appearance of the deformation structure is maintained, i.e. pronounced planar dislocation slip is observed indicating a very low cross slip frequency. A further refined planar dislocation structure is observed at a true strain of $\epsilon = 0.27$ (Fig. 3e). The slip bands are very closely spaced and start to be curved due to the high plastic strain. As shown in Fig. 3f, the deformation structure at $\epsilon = 0.34$ is characterized by further refinement of the above described slip band structure and an increased fraction of intersecting slip bands.

The overall evolution of the deformation structure is thus characterized by pronounced planar dislocation glide indicating a low cross slip frequency. Strong gradual refinement of the planar dislocation structure during straining is observed, whereas no deformation twins were detected in the deformation structure. Fig. 4 shows typical TEM bright-field micrographs and corresponding selected area diffraction patterns after 0.14 true strain, Fig. 4a and after 0.27 true strain, Fig. 4b. The absence of twinning spots confirms that no deformation twins are formed. Dissociation of perfect dislocations into Shockley partials is not observed by ECCI within the resolution limit (in the order of 8–10 nm [49]). Further, due to the high SFE of 85 mJ m^{-2} dislocation dissociation is energetically unfavorable.

It is important to note that the dislocation density within the slip bands at the grain boundaries is comparable to the dislocation density within the slip bands in the grain interior. Dislocations apparently become stuck within the grain interior rather than freely gliding towards the grain boundaries.

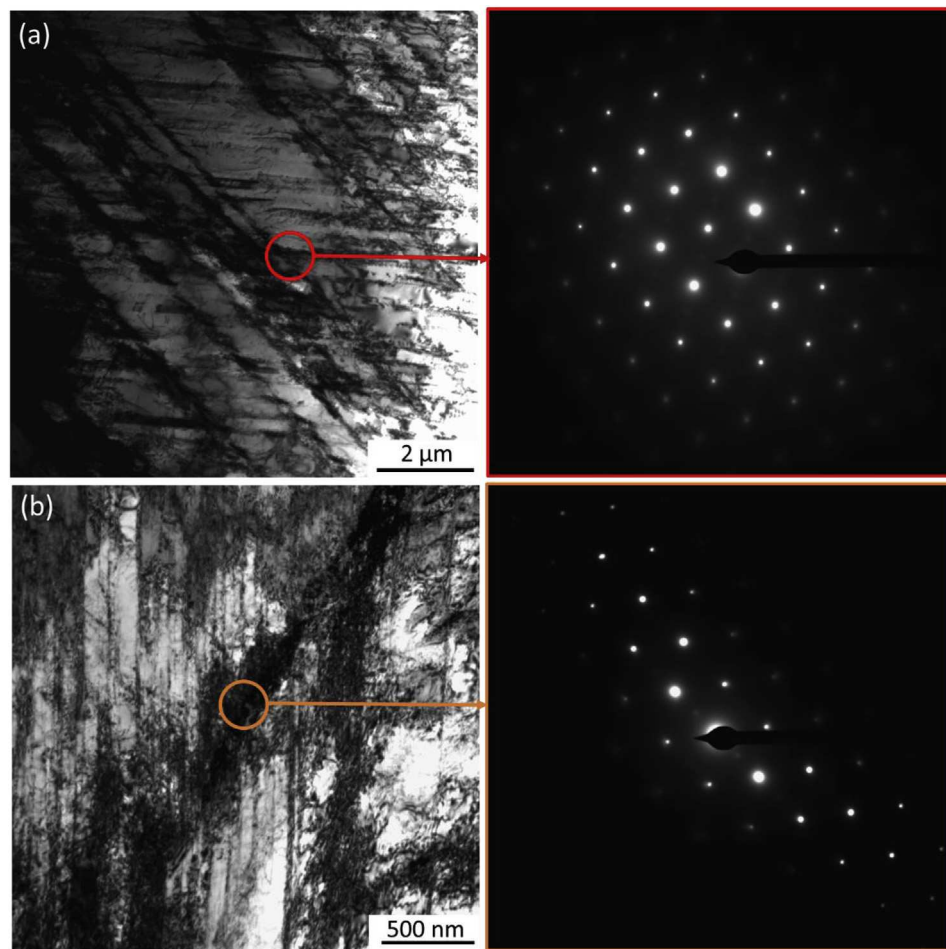


Fig. 4. Typical TEM bright-field micrographs and selected area diffraction patterns of the [110]-zone axis at different true strains ((a) $\epsilon = 0.14$ and (b) $\epsilon = 0.27$). The absence of twinning spots proves that no deformation twins are present in the deformation substructure.

3.4. Dislocation pile-ups and in-plane dislocation pairing at the slip band front

It is observed that slip bands typically extend throughout the grains until they impinge the grain boundaries. Slip bands ending within grains are only rarely observed. Features at the slip band front however, give valuable insights into the interaction between dislocations and the LRO-clusters presented in section 3.2. Here we focus on the dislocation configuration at the front of the slip bands.

Fig. 5a shows the deformation structure at $\epsilon = 0.02$. Several slip bands are observed on two non-coplanar {111} planes, as indicated by the slip plane traces. The arrows mark the front of the slip bands. The entire grain was carefully examined in order to make sure that no dislocations are present on the respective glide plane in propagation direction, which ensures the correct identification of the slip band front.

Fig. 5b displays the distances between neighboring perfect dislocations at the slip band front. The interspacing between the first and the second dislocation is referred to as ‘interspacing I’, the spacing between the second and the third dislocation as ‘interspacing II’ and so on. The dislocations are enumerated according to their position in the pile-up, starting at the slip band front with the first dislocation. The general trend of the inter-dislocation spacing reveals that the spacing among the dislocations decreases towards the slip band front, indicating a pile-up of dislocations towards the first dislocation of the slip band, however, without any apparent obstacle in its way.

More specific, the pile-up is characterized by a paired arrangement of dislocations, where subsets of two dislocations approach closer and leave a larger gap to the next pair. For instance Fig. 5b shows that the interspacing between the first and the second dislocation (interspacing I) is about 20 nm, whereas interspacing II to the next pair is about 100 nm wide. However, interspacing III, between the third and the fourth dislocation, is with about 23 nm smaller again, constituting a second pair. Interspacing IV is with a value of about 90 nm larger than interspacing III, whereas interspacing V is smaller (about 43 nm) than interspacing IV again, constituting a third pair. This pairing of consecutive dislocations in the pile-up is only observed for the first six dislocations, while the proceeding dislocations inside the pile-up do not show pair formation. They exhibit either equal or random spacings that are mainly governed by long-range stresses originating from surrounding dislocations and by local fluctuations of the friction stress. The observation of alternating dislocation spacings at the slip band front is a characteristic feature of freshly expanding slip bands in the present alloy (see also the inset in Fig. 3a and b).

3.5. Quantification of dynamic slip band refinement

In order to quantify the evolution of the slip band spacing during straining, at each investigated true strain level ($\epsilon = 0.02, 0.05, 0.14, 0.27, 0.34$) a representative number of grains was studied by ECCI. The measurements were conducted at different areas in the grains and an average slip band spacing D^* was derived from about 60

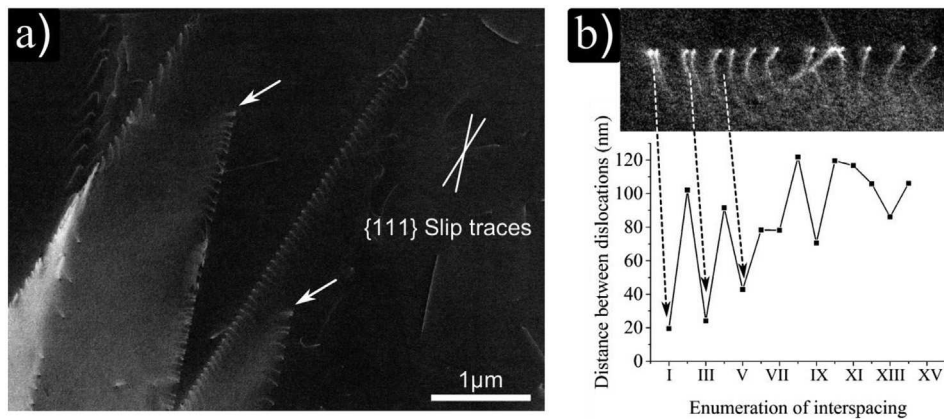


Fig. 5. Dislocation pile-ups at the slip band front. In (a) slip bands expand into a grain in a sample strained to $\epsilon = 0.02$ true strain. In (b) quantification of the dislocation distances closer to the tip of a freshly formed dislocation pile-up reveals clear pairing of the first six dislocations within the pile-up.

measurements per deformation state. Using EBSD the values for the slip band spacing were corrected regarding the inclination of the glide planes to the sample surface using the equation $D = \sin(\beta) \cdots D^*$, where β is the inclination angle of the slip band to the sample surface (see inset in Fig. 6).

The gradual refinement of the deformation substructure, which was already observed qualitatively in Fig. 3, is clearly revealed in Fig. 6 in terms of a decreasing mean slip band spacing with increasing strain. The error bars in the measurements (see markers in Fig. 6) are associated with the inhomogeneity of the deformation substructure, originating mainly from locally varying stress states within the sample [57–60].

4. Discussion

4.1. Parameters governing planar dislocation glide

The microstructure evolution of the studied alloy during straining is characterized by pronounced planar dislocation glide leading to the formation of crystallographic slip bands. The origin of pronounced planar glide in the FeMnAlC system was controversially discussed in the literature [24,46,61]. Three main reasons

for pronounced planar glide in fcc metals were proposed:

- 1) A low SFE leads to the splitting of perfect dislocations into Shockley partials, preventing dislocation cross slip. Large dissociation widths therefore reduce the cross slip frequency, hence, leading to planar glide. As the equilibrium distance between the dislocation partials increases with decreasing SFE, low SFEs promote planar glide [62].
- 2) In materials with high friction stresses, the critical resolved shear stress acting on a single dislocation might not be sufficiently high to overcome the threshold stress required for gliding. In this case the “stress multiplication effect” [63] enables collective glide of dislocations on the same glide plane. When dislocations glide in groups on the same plane, the first dislocation experiences the friction force of the crystal and the resolved stress from all following dislocations acting on it. As the succeeding dislocations push against the first one, the resolved shear stresses sum up, leading to an increased driving force to glide. The threshold stress can, therefore, be overcome by collective glide, which leads to slip planarity [31,64].
- 3) The presence of short range order (SRO) in a crystal increases the stress required for a dislocation to glide compared to the disordered state. When a dislocation propagates on a glide plane it destroys the SRO, facilitating propagation of succeeding dislocations on the same glide plane. As the glide plane is softened by the first dislocation, the phenomenon is consequently referred to as “glide plane softening”. The succeeding dislocations follow the preceding dislocation on its glide plane, hence promoting planar glide [32,65,66]. Gerold et al. [28] reported that shearable ordered precipitates lead to planar glide in a similar fashion.

The SFE in the material studied amounts to about 85 mJ m^{-2} [47], which is higher than in other fcc metals exhibiting non-planar dislocation glide such as copper ($\sim 60 \text{ mJ m}^{-2}$ [67]). In a similar FeMnC alloy with a lower SFE wavy slip was observed [3]. The SFE and the associated dislocation dissociation into partials can thus not account for the pronounced planar slip character which is observed in the current material.

Previous investigations proposed SRO to be present in similar alloys, leading to planar dislocation glide [30,61]. SRO is generally quite difficult to prove. To the authors' best knowledge no work is published in the literature so far confirming SRO experimentally in high-Mn lightweight steels. However, some works investigated SRO in high-Mn steels by DFT-simulations indicating SRO to be present [34–36,68].

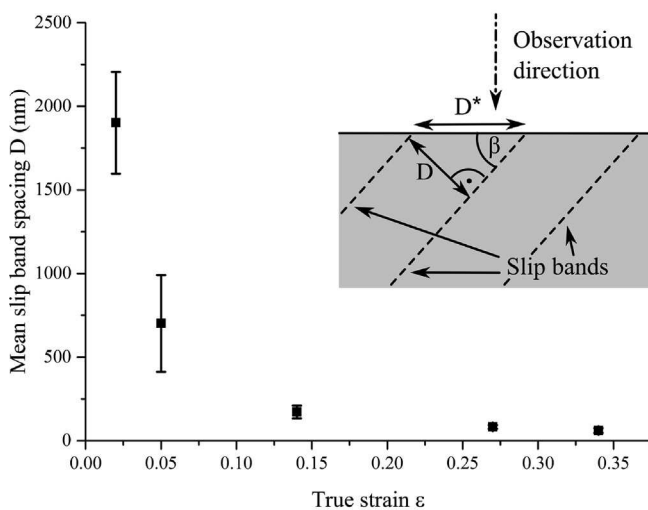


Fig. 6. Quantification of the evolution of the average slip band spacing during tensile straining. The substructure refinement is characterized by a decreasing mean slip band spacing. These values are used to calculate the flow stress as shown in the ensuing section in Fig. 6. The inset schematically illustrates the geometry and inclination correction applied.

Investigations on Ni-base alloys revealed the existence of SRO by means of diffuse neutron scattering [69], and its strong influence on the dislocation glide mode [70–72]. The authors showed how the preceding dislocations within a pile-up destroy the SRO and that succeeding dislocations which follow on the same glide plane produce pile-ups behind the leading one without the presence of other apparent obstacles. These earlier findings are similar to features presented in this work in section 3.4, which is an indication for SRO in the present material.

In the current alloy we observed the pairing of the first six dislocations within pile-ups at the slip band front. The reason for such dislocation pairing on the same glide plane is reported to be long range order (LRO) with a periodicity of twice the Burgers vector in Ni- and Co-based alloys [73–76]. The first dislocation of a dislocation pair destroys the LRO leaving an antiphase boundary behind whereas the succeeding dislocation restores the LRO. The attractive force due to the antiphase boundary (APB) leads to a small interspacing between the two dislocations inducing pairing. As the second dislocation restores the LRO, the third dislocation has to destroy the LRO again, causing periodic pairing of dislocations. It is, therefore, assumed that the observed LRO-clusters, see Fig. 2b, give rise to the pairing of the dislocations, as revealed in Fig. 5. Typically, the first six dislocations within a pile-up are paired, while the following dislocations seem not to be affected by LRO. From the number of paired dislocations the size of the sheared zones can be estimated. Once the ordered regions are completely sheared, no APB is generated any longer by further dislocations that pass [28]. Therefore, after the passage of six dislocations the ordered zones are fully sheared. The number of paired dislocations times the Burgers vector, hence, gives the size of the LRO-clusters. With a magnitude of the Burgers vector of $b = 0.26$ nm [45,77] the size of the LRO-clusters is estimated to be 1.6 nm. This value agrees well with the TEM observations given above where the LRO-cluster size was found to be lower than 2 nm (Fig. 2). The LRO-clusters are hence proven to influence the formation of slip bands due to the glide plane softening phenomenon originating from shearing of the LRO-clusters. Due to the small size of the sheared LRO-clusters, fringe contrast of APBs is not observable with ECCI (resolution limit of ECCI is in the order of 8–10 nm [49]).

Gerold et al. [28] reported that SRO as well as small shearable precipitates can promote planar dislocation glide. Therefore, we assume that the superposition of both, SRO and shearable LRO-clusters cause planar dislocation glide in the present alloy. These findings are in agreement with observations reported in Refs. [15,45] where small shearable precipitates are proposed to cause planar slip in a similar FeMnAlC-alloy and in Ref. [63] where both, SRO and 2 nm sized LRO clusters were observed in a Ni-base superalloy.

4.2. Effect of dynamic slip band refinement on strain hardening

The deformation microstructure of the FeMnAlC alloy exhibits pronounced planar dislocation arrangements throughout plastic straining. Neither strain-induced phase transformation, nor deformation twinning was observed during straining. The deformation substructure in the deformed material solely consists of dislocations, which renders it a “dislocation-mediated plasticity” alloy [78]. Hence, the reason for the excellent strain hardening properties is attributed to the gradual deformation-driven refinement of the slip band substructure. The decreasing slip band spacing observed is regarded as the main structural parameter that characterizes the deformation microstructure evolution. In the following calculation we thus used the quantification of the mean slip band spacing evolution (Fig. 6) to derive the flow stress from the microstructure. The total flow stress, σ_{tot} , in dislocation-mediated plasticity

materials is approximated by different contributions that can be expressed in the following equation [79,80]:

$$\sigma_{\text{tot}} = \sigma_F + \sigma_{\text{SS}} + \sigma_{\text{GB}} + \sigma_P + \sigma_{\text{SRO}} + \sigma_{\text{SH}}(\epsilon) \quad (1)$$

here σ_F is the Peierls-Nabarro lattice friction stress, σ_{SS} is the contribution of alloying elements in solid solution, σ_{GB} is the Hall-Petch strengthening due to grain boundaries, σ_P and σ_{SRO} are the stress contributions due to precipitates and short range order, respectively. The last term $\sigma_{\text{SH}}(\epsilon)$ (SH: strain hardening) includes the influence of strain hardening mechanisms that evolve upon mechanical loading. In the present material mainly dislocation-dislocation interactions contribute to this latter term.

These contributions can be grouped into deformation-dependent strengthening mechanisms $\sigma_{\text{SH}}(\epsilon)$ and those that do not depend on the deformation, summarized in σ_0 . The yield stress depends on σ_0 , whereas the strain hardening term $\sigma_{\text{SH}}(\epsilon)$ describes changes of the flow stress during progressing plastic deformation. The total flow stress, therefore, falls into two contributions [79,81,82]:

$$\sigma_{\text{tot}}(\epsilon) = \sigma_0 + \sigma_{\text{SH}}(\epsilon) \quad (2)$$

The strain hardening contribution due to the refinement of the slip band structure is derived by the passing stress [25,26,64,83–85] as follows:

$$\sigma_{\text{SH}}(\epsilon) = K \cdot M \cdot G \cdot b / D \quad (3)$$

where K is a geometrical factor, $M = 3.06$ is the Taylor-factor for randomly distributed grain orientations, $G = 70$ GPa [77,86,87] is the bulk elastic shear modulus of the alloy, $b = 0.26$ nm is the magnitude of the Burgers vector [45,77,87] and D is the mean slip band spacing (see Fig. 6).

Fig. 7 shows the true stress-true strain curve for the tensile test (solid line) along with the calculated stress values (squares), which are derived by using equations (2) and (3) in conjunction with the results of the slip band analysis in Fig. 6. The calculated stresses reproduce the values from the experimentally determined tensile test curve with good agreement. Especially the measured and calculated nearly constant strain hardening rates both confirm that

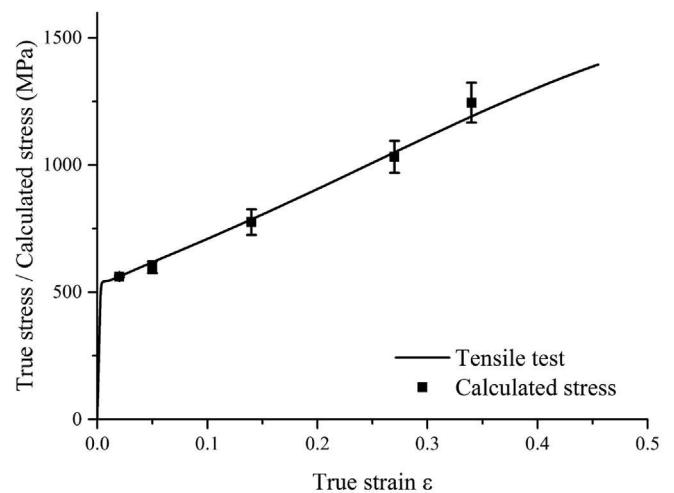


Fig. 7. Measured true stress-true strain curve (solid line) and calculated stress values (squares). The calculated values are derived using the results of the microstructure analysis shown in Fig. 6 in conjunction with equations (2) and (3). The nearly linear strain hardening behavior is attributed to the microstructure refinement. The reduced slip band spacing during straining explains the flow stress and is therefore regarded as the main structural parameter governing the strain hardening behavior.

slip band refinement is indeed the governing structural parameter leading to the observed material properties. The best fit between experiment and calculation is achieved when using a K -value of 0.7 and a σ_0 -value of 540 MPa. The small difference between σ_0 and the experimental yield strength σ_{Yield} (550 MPa), arises from the small drop of the work hardening rate after the onset of yielding.

Microstructure refinement was frequently used in the past in order to link the microstructural evolution with the flow stress [3,46,81,88]. However, it has not yet been shown that crystallographically aligned slip bands, such as observed in the current study, can have a similar effect on the strain hardening behavior. Based on the agreement between the measured true stress-true strain curves and the calculated stress values, we conclude that the slip band spacing is the main microstructural parameter that links the evolution of the deformation structure on the micrometer scale to the macroscopic flow stress, although an additional contribution by hindering the intersection of dislocations through slip bands cannot be totally excluded.

It should be emphasized that the underlying strengthening mechanism behind equation (3) is assumed to be mainly due to the long range elastic interactions among slip bands on co-planar glide planes due to the stress fields created by the dislocations. There has been some debate in the past whether long range stresses, in particular the passing stress [89], or short range stresses such as cutting stresses (stress originating from the dislocation cutting process) represent the main strengthening contribution in dislocation-mediated materials [25,26,89–91]. As both mechanisms show the same dependence on the microstructural parameter D it is difficult to distinguish between them in the current study. However, as slip bands that are blocked by intersecting slip bands or pile-ups at intersecting slip bands are only rarely observed, we suggest that intersecting slip bands do not significantly obstruct each other at intersection lines, which would be expected in the case of the formation of Lomer-Cottrell-locks or strong resistance to dislocation shearing. Thus, long-range stresses originating from the stored slip bands are assumed to be the main contribution to strain hardening in the studied alloy rather than cutting of intersecting slip bands.

This is in contradiction to the earlier proposed strain hardening mechanism that was suggested to proceed via formation of microbands (MBIP), the associated grain subdivision [23] and the resulting Hall-Petch-type hardening effect [92]. As opposed to this model assumption the detailed study conducted here by using ECCI does not show any signs of double walled microbands that obstruct dislocation glide, but solely proves the formation of slip bands that reach throughout entire grains. It is thus concluded that the novel strain hardening by dynamic slip bands refinement provides a convincing explanation of the observed outstanding strain hardening behavior.

The yield stress σ_{Yield} of 550 MPa is considerably higher than in similar alloys with a lower aluminum content (i.e. 420 MPa in Fe-30.5Mn-2.1Al-1.2C (wt%) [46]), which may be attributed to the higher friction stresses due to SRO and the LRO-clusters present in the current alloy and to a small extend also to solid solution strengthening.

4.3. Discussion of the microstructure evolution: dynamic slip band refinement as a strain hardening mechanism

The results of the preceding section reveal that the microstructural evolution is characterized by the formation of slip bands due to pronounced planar dislocation glide. The refinement of this characteristic microstructure during straining is found to be the key parameter governing the strain hardening behavior in the alloy investigated. In the following we discuss the formation of the

observed deformation structure and its influence on the macroscopic properties such as ductility, strength and strain hardening capacity.

Fig. 8 schematically shows the evolution of the deformation substructure during straining in one representative grain. At the onset of plastic deformation dislocation sources in the form of Frank-Read sources and grain boundary sources start to emit dislocations. Accommodation of plastic strain in a polycrystal requires activation of several, non-coplanar slip systems (according to the Taylor – von-Mises compatibility criterion at least 5 independent systems are required but, if grains are small enough, 3 or 4 are sufficient at moderate strains). This means that crossing slip (non-coplanar) slip systems will be activated already at low strains of 0.02–0.05 as suggested by Figs. 3c and 5a. As the dislocations interact with each other and with the ordered clusters, additional dislocation sources start to operate by cross slip associated with the well-established Frank-Read bow-out mechanism, forming loops that expand and leave the source (Fig. 8a). Such Frank-Read sources [93] are experimentally observed in the studied material, see inset in Fig. 3a and arrows in Fig. 3b. The presence of SRO and finely dispersed LRO-clusters increases the stresses needed to bow out single dislocations, compared to the disordered crystal. The dislocation loops expand and leave the Frank-Read sources, thereby destroying any kind of compositional order (be it SRO or LRO-clusters) present on its glide plane. This process causes softening of the glide plane which facilitates the generation of new dislocation loops following from the same source. Activated Frank-Read sources can therefore readily generate a large number of dislocations on the same glide plane. Such a glide plane softening phenomenon which was reported before [2,22,28,30,32] is applied here to Frank-Read sources explaining the initiation of slip bands. As pointed out in section 4.1, glide plane softening is also associated with the occurrence of pile-ups without the apparent presence of obstacles, as shown in Fig. 5. The stress multiplication effect further helps overcoming high friction stresses by the collective glide of groups of dislocations [63,94].

Dislocations propagating in groups within the slip bands (e.g. Fig. 3a, b and c) are explained by fluctuations of SRO and LRO and more importantly by long-range stresses originating from already stored slip bands. As the passing stress is shown to be the main contribution to strain hardening, see section 4.2, closely spaced slip bands will indeed mutually exert strong effects on the dislocation distribution assembled in the slip bands [84,95–98]. Similar observations are given in Ref. [26] where ‘dislocation trains’ gliding through the crystal have been reported.

The emitted dislocations eventually reach the grain boundaries or become mutually trapped in the grain interior by dislocations on parallel slip bands. As the generated dislocations do only rarely leave their glide plane, which is related to the pronounced order-induced planar slip behavior, the glide plane fills up with dislocations, see Fig. 8b. These piled-up dislocations eventually lead to back stresses acting on the source, which increases with the number of emitted dislocations. Once the local stress at the source falls below the critical activation stress, the source ceases to emit further dislocation loops. In this situation the slip plane is filled with dislocations appearing as slip bands throughout the grain, as experimentally observed, see section 3.3. The slip band can be regarded as fully developed, as the generation of dislocations within the slip band is strongly inhibited, see dotted line in Fig. 8c. It is important to note that initially glide plane softening induces the formation of slip bands, but as the dislocation density within the slip band increases, the mentioned back stresses eventually cause glide plane hardening, which is the reason for the exhaustion of the source and, hence, for the termination of the individual slip band evolution (Fig. 8b).

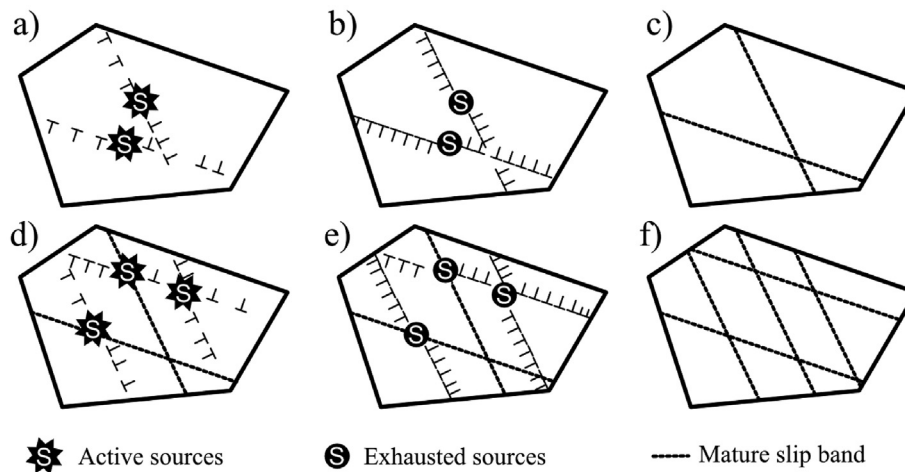


Fig. 8. Schematic illustration of the proposed dynamic slip band refinement. (a) Activation of sources. (b) Slip planes fill-up with dislocations. (c) Sources become exhausted due to back stresses. Slip bands are fully developed (indicated by dotted lines). (d) Activation of new sources is necessary. (e–f) Newly activated sources will undergo the same evolution as the previous sources. The described process explains the observed refinement of the slip band substructure.

In order to further accommodate plastic strain the generation of more dislocations is necessary (Fig. 8d). New sources get activated, most likely in the already present non-coplanar slip bands either by mutual shearing of slip bands as pointed out in Ref. [91], by rare dislocation cross slip events initiating new slip bands [99] or by the activation of already existing sources that require higher activation stress due to smaller segment length L in accord with Orowan's law ($\sigma_{\text{Orowan}} \sim 1/L$) [100,101]. These new sources again produce expanding dislocation loops on their respective glide planes, which induces the formation of more slip bands leading to a refinement of the slip band substructure (Fig. 8e,f). Hence, the spacing between the slip bands reduces during straining. The increasing number of slip bands leads to a strong increase in the stored dislocation density that contributes to strain hardening mainly due to the higher passing stress caused by the reduced slip band spacing and to a small extend by a higher frequency of dislocation cutting, as pointed out in section 4.2.

As this process continuously proceeds, it results in high elongations and a constant strain hardening rate. However, when the critical lowest spacing between slip bands is reached, which occurs when dislocations on parallel slip bands are close enough to annihilate, or the increasing stress enables cross slip [46], the rate of dislocation generation strongly reduces. This dynamic recovery of the band structure leads to a drop in strain hardening rate and eventually to plastic failure, as indicated in the Considère-plot in Fig. 1.

The outlined mechanism readily explains the planar slip character of the substructure evolution observed by ECCI in section 3.3 and hence the formation of slip bands during straining. The corresponding calculations show the potential of the substructure evolution to cause the high nearly constant strain hardening rate and also the excellent combination of strength and ductility of this high-Mn steel, see section 4.2.

The observation that slip bands mostly extend through entire grains (see Fig. 3) indicates that once a source is activated the corresponding slip band quickly evolves until the source is exhausted. This observation is interpreted such that the glide plane softening due to the destruction of SRO and LRO-clusters causes a quick slip band evolution, which supports the suggested slip band formation.

The described deformation mechanism and strain hardening mechanism can be interpreted in the framework of the classical

deformation stages for fcc metals [90]. While stage I (easy glide regime) is only present in single crystals, stage II and stage III prevail in polycrystals. Stage II-strain hardening is characterized by a strong monotonic increase of the stored dislocation density without dynamic recovery, leading to a constant strain hardening rate. In the present alloy the dislocation density increases monotonically due to the generation of new slip bands during straining. The mean slip band spacing has been evaluated statistically in the present study (Fig. 6) and shown to lead to a nearly constant strain hardening rate. The stored slip bands comprise the stored dislocation density which increases with increasing strain. What is essential in the current alloy is that the transition from stage II to stage III is shifted to higher strains due to suppressed cross slip activity compared to other fcc metals [90]. As planar slip is strongly promoted, the low cross slip activity reduces the ability for dislocation annihilation, which would lead to dynamic recovery [79,102]. Therefore the dislocation density increases during straining monotonically leading to a nearly constant strain hardening rate from the onset of plastic deformation until failure. Interestingly, similar conclusions were drawn for an ordered bcc FeCo-alloy before [103].

The essential characteristics of the described mechanism are the gradual deformation-driven refinement of the slip band substructure and the suppression of catastrophic strain localization which is often observed in other planar slip materials. The fundamental reason for such a behavior is the strengthening of the grain-internal dislocation structure via long-range stresses preventing high local stresses at the grain boundary. As mentioned in section 3.3 the dislocation density is homogeneously distributed within the grains, suggesting that hardening of the grain interior by mutual trapping of dislocations on parallel slip bands plays an important role. While glide plane softening induces the formation of slip bands on parallel glide planes, which would subsequently lead to catastrophic failure along such bands, the successive hardening of slip bands leads to an exhaustion of the respective source, which stops further evolution of the slip band, preventing excessive softening and failure. Hence, high localized strains on one slip plane are suppressed, which otherwise would lead to the formation of cracks at the grain boundary leading to premature failure. The pronounced planar glide prevents hereby the broadening of slip bands, which also can lead to increasing local stresses at the grain boundary, but instead induces the refinement of the substructure by generating new slip

band in the free space between the existing ones. The observed dynamic slip band refinement is hence related to fine planar slip. While broadening of slip bands would lead to “coarse planar slip”. As a consequence dynamic slip band refinement leads to high ductility and high strain hardening.

5. Conclusions

In this study we investigated the microstructural evolution during straining of a high-Mn steel (Fe-30.4Mn-8Al-1.2C (wt%)) by means of TEM, ECCI and EBSD. ECCI analysis was performed at different strain levels in order to track the microstructure development, while TEM investigation was conducted to investigate the precipitation state. The following conclusions are drawn:

- The investigated steel exhibits an outstanding combination of strength and ductility. The high strain hardening rate of approximately 2000 MPa leads to 1440 MPa true stress at a uniform true strain of 0.46 (i.e. UTS of 900 MPa, UE of 60% and TE of 68%).
- The deformation microstructure is characterized by pronounced planar slip. Neither deformation twins nor phase transformations were observed during straining. The material therefore falls into the group of dislocation-mediated plasticity steels [78]. Strong slip planarity leads to the formation of very thin slip bands that expand through the entire grain. The slip band structure undergoes refinement during straining, reducing the spacing between the slip bands. The deformation mechanism is therefore regarded as dynamic slip band refinement.
- The evolution of the slip band spacing is found to be the key parameter governing the strain hardening behavior. The measured slip band spacing is connected to the flow stress via the passing stress. The good agreement between the calculated stress values and the flows stress obtained from the tensile test shows that the observed nearly linear strain hardening behavior can be explained by the dynamic slip band refinement in conjunction with passing stresses. It should be emphasized that the presented novel strain hardening mechanism is first described in the framework of this study.
- Pile-ups of dislocations were found at the front of the expanding slip bands. This observation is attributed to the presence of SRO and the shearing process of nano-sized (<2 nm) long-range-ordered clusters (LRO-clusters) that are observed in the as-quenched state giving rise to glide plane softening.
- The LRO-clusters induce dislocation pairing at the slip band front. The first six dislocations within a pile-up are paired due to the antiphase boundary (APB) that is created between two succeeding dislocations. The APB is the result of the sheared LRO-clusters. The size of the sheared zones was estimated based on the number of paired dislocations within a pile-up. The estimated size of about 1.6 nm is in good agreement with the TEM results showing LRO-clusters of less than 2 nm in size.
- In the framework of the well-known deformation stages in fcc alloys, the low cross-slip frequency leads to a shift of the transition from stage-II to stage-III towards higher strains. Pronounced planar slip impedes annihilation of dislocations. As dynamic recovery is hence suppressed the dislocation density increases monotonically leading to a constant strain hardening rate. The investigated steel can therefore be regarded as “stage-II-hardening alloy” [79,102].

Acknowledgements

We acknowledge Jiali Zhang for the kind help with the TEM work. D. P., D. R., M. H., St. S., S. Z. gratefully acknowledge funding by

the Deutsche Forschungsgemeinschaft (DFG), Germany, through the collaborative research center SFB 761 ‘Steel ab initio’.

References

- [1] O. Grässel, et al., High strength Fe–Mn–(Al, Si) TRIP/TWIP steels development-properties-application, *Int. J. Plast.* 16 (10–11) (2000) 1391–1409.
- [2] J.D. Yoo, K.-T. Park, Microband-induced plasticity in a high Mn–Al–C light steel, *Mater. Sci. Eng. A* 496 (1–2) (2008) 417–424.
- [3] I. Gutierrez-Urrutia, D. Raabe, Dislocation and twin substructure evolution during strain hardening of an Fe–22wt% Mn–0.6wt% C TWIP steel observed by electron channeling contrast imaging, *Acta Mater.* 59 (16) (2011) 6449–6462.
- [4] J.-K. Kim, et al., Strain rate sensitivity of C-alloyed, high-Mn, twinning-induced plasticity steel, *Steel Res. Int.* 80 (7) (2009) 493–498.
- [5] S. Curtze, V.T. Kuokkala, Dependence of tensile deformation behavior of TWIP steels on stacking fault energy, temperature and strain rate, *Acta Mater.* 58 (15) (2010) 5129–5141.
- [6] H. Idrissi, et al., On the relationship between the twin internal structure and the work-hardening rate of TWIP steels, *Scr. Mater.* 63 (10) (2010) 961–964.
- [7] O. Bouaziz, et al., High manganese austenitic twinning induced plasticity steels: a review of the microstructure properties relationships, *Curr. Opin. Solid State Mater. Sci.* 15 (4) (2011) 141–168.
- [8] J.E. Jin, Y.K. Lee, Effects of Al on microstructure and tensile properties of C-bearing high Mn TWIP steel, *Acta Mater.* 60 (4) (2012) 1680–1688.
- [9] J.S. Jeong, et al., In situ neutron diffraction study of the microstructure and tensile deformation behavior in Al-added high manganese austenitic steels, *Acta Mater.* 60 (5) (2012) 2290–2299.
- [10] G.A.U.B. Frommeyer, Microstructures and mechanical properties of high-strength Fe–Mn–Al–C light-weight TRIPLEX steels, *Steel Res. Int.* 77 (9–10) (2006) 627–633.
- [11] D. Raabe, et al., Alloy design, combinatorial synthesis, and microstructure–property relations for low-density Fe–Mn–Al–C austenitic steels, *JOM* (2014) 1–12.
- [12] H. Springer, D. Raabe, Rapid alloy prototyping: compositional and thermo-mechanical high throughput bulk combinatorial design of structural materials based on the example of 30Mn–1.2C–xAl triplex steels, *Acta Mater.* 60 (12) (2012) 4950–4959.
- [13] D.T. Pierce, et al., The influence of manganese content on the stacking fault and austenite/ε-martensite interfacial energies in Fe–Mn–(Al–Si) steels investigated by experiment and theory, *Acta Mater.* 68 (2014) 238–253.
- [14] D.T. Pierce, et al., The influence of stacking fault energy on the microstructural and strain-hardening evolution of Fe–Mn–Al–Si steels during tensile deformation, *Acta Mater.* 100 (2015) 178–190.
- [15] K. Choi, et al., Effect of aging on the microstructure and deformation behavior of austenite base lightweight Fe–28Mn–9Al–0.8C steel, *Scr. Mater.* 63 (10) (2010) 1028–1031.
- [16] H. Kim, D.-W. Suh, N.J. Kim, Fe–Al–Mn–C lightweight structural alloys: a review on the microstructures and mechanical properties, *Sci. Technol. Adv. Mater.* 14 (1) (2013) 014205.
- [17] C.-H. Seo, et al., Deformation behavior of ferrite–austenite duplex lightweight Fe–Mn–Al–C steel, *Scr. Mater.* 66 (8) (2012) 519–522.
- [18] J.-B. Seol, et al., Direct evidence for the formation of ordered carbides in a ferrite-based low-density Fe–Mn–Al–C alloy studied by transmission electron microscopy and atom probe tomography, *Scr. Mater.* 68 (6) (2013) 348–353.
- [19] J.-E. Jin, Y.-K. Lee, Strain hardening behavior of a Fe–18Mn–0.6C–1.5Al TWIP steel, *Mater. Sci. Eng. A* 527 (1–2) (2009) 157–161.
- [20] J.K. Kim, et al., On the tensile behavior of high-manganese twinning-induced plasticity steel, *Metall. Mater. Trans. A Phys. Metall. Mater. Sci.* 40A (13) (2009) 3147–3158.
- [21] I. Gutierrez-Urrutia, S. Zaefferer, D. Raabe, The effect of grain size and grain orientation on deformation twinning in a Fe–22wt% Mn–0.6wt% C TWIP steel, *Mater. Sci. Eng. A* 527 (15) (2010) 3552–3560.
- [22] K.-T. Park, Tensile deformation of low-density Fe–Mn–Al–C austenitic steels at ambient temperature, *Scr. Mater.* 68 (6) (2013) 375–379.
- [23] J.D. Yoo, S.W. Hwang, K.T. Park, Origin of extended tensile ductility of a Fe–28Mn–10Al–1C steel, *Metall. Mater. Trans. A* 40 (7) (2009) 1520–1523.
- [24] K.-T. Park, et al., On the transitions of deformation modes of fully austenitic steels at room temperature, *Metals Mater. Int.* 16 (1) (2010) 1–6.
- [25] C.S. Pande, P.M. Hazzledine, Dislocation arrays in Cu–Al alloys. I, *Philos. Mag.* 24 (191) (1971) 1039–1057.
- [26] C.S. Pande, P.M. Hazzledine, Dislocation arrays in Cu–Al alloys. II, *Philos. Mag.* 24 (192) (1971) 1393–1410.
- [27] T. Steffens, et al., Transmission electron microscopy study of the stacking-fault energy and dislocation structure in CuMn alloys, *Philos. Mag. A* 56 (2) (1987) 161–173.
- [28] V. Gerold, H.P. Karnthaler, On the origin of planar slip in f.c.c. alloys, *Acta Metall.* 37 (8) (1989) 2177–2183.
- [29] S.I. Hong, C. Laird, Mechanisms of slip mode modification in F.C.C. solid solutions, *Acta Metall. Metall.* 38 (8) (1990) 1581–1594.
- [30] K.-T. Park, et al., Stacking fault energy and plastic deformation of fully austenitic high manganese steels: effect of Al addition, *Mater. Sci. Eng. A* 527

- (16–17) (2010) 3651–3661.
- [31] J. Olfe, H. Neuhäuser, Dislocation groups, multipoles, and friction stresses in α -CuZn alloys, *Phys. Status Solidi (A)* 109 (1) (1988) 149–160.
 - [32] G. Saller, et al., Microstructural evolution of Cr–Mn–N austenitic steels during cold work hardening, *Mater. Sci. Eng. A* 427 (1–2) (2006) 246–254.
 - [33] S.C. Tjong, Electron microscope observations of phase decompositions in an austenitic Fe–8.7Al–29.7Mn–1.04C alloy, *Mater. Charact.* 24 (3) (1990) 275–292.
 - [34] J.-H. Kang, et al., Impact of short-range ordering on yield strength of high manganese austenitic steels, *Mater. Sci. Eng. A* 614 (0) (2014) 122–128.
 - [35] J. von Appen, R. Dronskowski, Carbon-induced ordering in manganese-rich austenite — a density-functional total-energy and chemical-bonding study, *Steel Res. Int.* 82 (2) (2011) 101–107.
 - [36] M. Kang, et al., Small-angle neutron scattering analysis of Mn–C clusters in high-manganese 18Mn–0.6C steel, *Mater. Charact.* 96 (0) (2014) 40–45.
 - [37] M. Palm, G. Inden, Experimental determination of phase equilibria in the FeAlC system, *Intermetallics* 3 (6) (1995) 443–454.
 - [38] M.J. Yao, et al., Combined atom probe tomography and density functional theory investigation of the Al off-stoichiometry of κ -carbides in an austenitic Fe–Mn–Al–C low density steel, *Acta Mater.* 106 (2016) 229–238.
 - [39] K. Sato, K. Tagawa, Y. Inoue, Spinodal decomposition and mechanical properties of an austenitic Fe–30wt%Mn–9wt%Al–0.9wt%C alloy, *Mater. Sci. Eng. A* 111 (0) (1989) 45–50.
 - [40] K. Sato, K. Tagawa, Y. Inoue, Modulated structure and magnetic properties of age-hardenable Fe–Mn–Al–C alloys, *Metall. Trans. A* 21 (1) (1990) 5–11.
 - [41] C.Y. Chao, L.K. Hwang, T.F. Liu, Spinodal decomposition in Fe₉₀Al₁₀Mn₉₀C alloys, *Scripta Metall. Metall.* 29 (5) (1993) 647–650.
 - [42] C.N. Hwang, C.Y. Chao, T.F. Liu, Grain boundary precipitation in an Fe–8.0Al–31.5Mn–1.05C alloy, *Scripta Metall. Metall.* 28 (2) (1993) 263–268.
 - [43] K.M. Chang, C.G. Chao, T.F. Liu, Excellent combination of strength and ductility in an Fe–9Al–28Mn–1.8C alloy, *Scr. Mater.* 63 (2) (2010) 162–165.
 - [44] Y. Kimura, et al., Microstructure control and ductility improvement of the two-phase γ -Fe/ κ -(Fe, Mn)3AlC alloys in the Fe–Mn–Al–C quaternary system, *Intermetallics* 12 (6) (2004) 607–617.
 - [45] W.K. Choo, J.H. Kim, J.C. Yoon, Microstructural change in austenitic Fe–30.0wt%Mn–7.8wt%Al–1.3wt%C initiated by spinodal decomposition and its influence on mechanical properties, *Acta Mater.* 45 (12) (1997) 4877–4885.
 - [46] I. Gutierrez-Urrutia, D. Raabe, Multistage strain hardening through dislocation substructure and twinning in a high strength and ductile weight-reduced Fe–Mn–Al–C steel, *Acta Mater.* 60 (16) (2012) 5791–5802.
 - [47] I. Gutierrez-Urrutia, D. Raabe, High strength and ductile low density austenitic FeMnAlC steels: simple and alloys strengthened by nanoscale ordered carbides, *Mater. Sci. Technol.* 30 (9) (2014) 1099–1104.
 - [48] I. Gutierrez-Urrutia, D. Raabe, Influence of Al content and precipitation state on the mechanical behavior of austenitic high-Mn low-density steels, *Scr. Mater.* 68 (6) (2013) 343–347.
 - [49] S. Zaefferer, N.-N. Elhami, Theory and application of electron channelling contrast imaging under controlled diffraction conditions, *Acta Mater.* 75 (2014) 20–50.
 - [50] D.R. Steinmetz, et al., Revealing the strain-hardening behavior of twinning-induced plasticity steels: theory, simulations, experiments, *Acta Mater.* 61 (2) (2013) 494–510.
 - [51] O. Bouaziz, Strain-hardening of twinning-induced plasticity steels, *Scr. Mater.* 66 (12) (2012) 982–985.
 - [52] K. Ishida, et al., Phase equilibria in Fe–Mn–Al–C alloys, *ISIJ Int.* 30 (8) (1990) 680–686.
 - [53] C.L. Lin, et al., Relationship between microstructures and tensile properties of an Fe–30Mn–8.5Al–2.0C Alloy, *Mater. Trans.* 51 (6) (2010) 1084–1088.
 - [54] K. Sato, K. Tagawa, Y. Inoue, Age hardening of an Fe–30Mn–9Al–0.9C alloy by spinodal decomposition, *Scr. Metall.* 22 (6) (1988) 899–902.
 - [55] D. Raabe, et al., Alloy design, combinatorial synthesis, and microstructure–property relations for low-density Fe–Mn–Al–C austenitic steels, *JOM* 66 (9) (2014) 1845–1856.
 - [56] H. Inui, S.I. Hong, C. Laird, A TEM study of dislocation structures in fatigued Cu–16 at.% Al single crystals, *Acta Metall. Metall.* 38 (11) (1990) 2261–2274.
 - [57] C.C. Tasan, et al., Integrated experimental–simulation analysis of stress and strain partitioning in multiphase alloys, *Acta Mater.* 81 (2014) 386–400.
 - [58] D. Raabe, et al., Micromechanical and macromechanical effects in grain scale polycrystal plasticity experimentation and simulation, *Acta Mater.* 49 (17) (2001) 3433–3441.
 - [59] Z. Zhao, et al., Investigation of three-dimensional aspects of grain-scale plastic surface deformation of an aluminum oligocrystal, *Int. J. Plast.* 24 (12) (2008) 2278–2297.
 - [60] M. Sachtler, Z. Zhao, D. Raabe, Experimental investigation of plastic grain interaction, *Mater. Sci. Eng. A* 336 (1–2) (2002) 81–87.
 - [61] J.D. Yoo, S.W. Hwang, K.-T. Park, Factors influencing the tensile behavior of a Fe–28Mn–9Al–0.8C steel, *Mater. Sci. Eng. A* 508 (1–2) (2009) 234–240.
 - [62] J.P. Hirth, J. Lothe, *Theory of Dislocations*, 1968, p. 696.
 - [63] M. Jouiad, N. Clément, A. Coujou, Friction stresses in the γ phase of a nickel-based superalloy, *Philos. Mag. A* 77 (3) (1998) 689–699.
 - [64] H. Neuhäuser, O.B. Arkan, H.H. Potthoff, Dislocation multipoles and estimation of frictional stress in f.c.c. copper alloys, *Mater. Sci. Eng.* 81 (0) (1986) 201–209.
 - [65] H. Roelofs, et al., Atomic short-range order in Cu–17 at.% Mn, *Phys. Status Solidi (B)* 187 (1) (1995) 31–42.
 - [66] F. Pettinari-Sturm, et al., Activation of dislocation sources in γ -phases of nickel-base superalloys studied by use of atomic-force microscopy and transmission electron microscopy, *Mater. Sci. Eng. A* 387–389 (0) (2004) 103–108.
 - [67] P. Heino, et al., Stacking-fault energy of copper from molecular-dynamics simulations, *Phys. Rev. B* 60 (21) (1999) 14625–14631.
 - [68] W. Song, et al., κ -Phase formation in Fe–Mn–Al–C austenitic steels, *Steel Res. Int.* (2015) n/a–n/a.
 - [69] F. Pettinari, et al., Local order in industrial and model γ phases of superalloys, *Acta Mater.* 49 (13) (2001) 2549–2556.
 - [70] F. Pettinari-Sturm, A. Coujou, N. Clément, The fluctuation of short-range order evidenced by mobile dislocations in the γ -phase of a nickel-based superalloy, *Mater. Sci. Eng. A* 400–401 (0) (2005) 114–117.
 - [71] F. Pettinari-Sturm, et al., Characterisation of short-range order using dislocations, *Z. für Met.* 97 (3) (2006) 200–204.
 - [72] F. Pettinari-Sturm, et al., Quantitative analysis of dislocation pile-ups in thin foils compared to bulk, *Mater. Sci. Eng. A* 387–389 (0) (2004) 109–114.
 - [73] G. Thomas, The effect of short-range order on stacking fault energy and dislocation arrangements in f.c.c. solid solutions, *Acta Metall.* 11 (12) (1963) 1369–1371.
 - [74] R. Glas, et al., Order and mechanical properties of the γ matrix of superalloys, *Acta Mater.* 44 (12) (1996) 4917–4926.
 - [75] A. Korner, Dislocation structures in disordered and ordered Ni₃Fe, *Acta Metall.* 33 (8) (1985) 1399–1406.
 - [76] Y. Liu, et al., TEM investigation of dislocation dissociation in L1₂-type Co₇₄Ni₂₆Ti₂₃ single crystals II. The influence of the deformation temperature, *Philos. Mag. A* 59 (2) (1989) 437–454.
 - [77] W. Choo, K. Han, Phase constitution and lattice parameter relationships in rapidly solidified (Fe_{0.65}Mn_{0.35})_{0.83}Al_{0.17}-x C and Fe₃Al-x C pseudo-binary alloys, *Metall. Trans. A* 16 (1) (1985) 5–10.
 - [78] D. Kuhlmann-Wilsdorf, Chapter 59 the LES theory of solid plasticity, in: F.R.N. Nabarro, M.S. Duesbery (Eds.), *Dislocations in Solids*, Elsevier, 2002, pp. 211–342.
 - [79] D. Kuhlmann-Wilsdorf, H.G.F. Wilsdorf, J.A. Wert, LEDS theory of work-hardening stages and “planar” versus “distributed” glide, *Scripta Metall. Metall.* 31 (6) (1994) 729–734.
 - [80] U.F. Kocks, H. Mecking, Physics and phenomenology of strain hardening: the FCC case, *Prog. Mater. Sci.* 48 (3) (2003) 171–273.
 - [81] X. Feaugas, On the origin of the tensile flow stress in the stainless steel AISI 316L at 300 K: back stress and effective stress, *Acta Mater.* 47 (13) (1999) 3617–3632.
 - [82] D. Kuhlmann-Wilsdorf, Theory of plastic deformation: – properties of low energy dislocation structures, *Mater. Sci. Eng. A* 113 (0) (1989) 1–41.
 - [83] N. Hansen, Cold deformed microstructures, *Mater. Sci. Technol.* 6 (1990) 1039.
 - [84] E. Smith, The by-passing of an obstacle by a group of coplanar dislocations, *Philos. Mag.* 22 (180) (1970) 1161–1173.
 - [85] H. Neuhäuser, Electron microscopic studies in the yield region of 70/30- α -brass single crystals—II. Estimation of the dislocation friction stress, *Acta Metall.* 23 (4) (1975) 455–462.
 - [86] J. Kim, B.C. De Cooman, On the stacking fault energy of Fe–18 Pct Mn–0.6 Pct C–1.5 Pct Al twinning-induced plasticity steel, *Metall. Mater. Trans. A* 42 (4) (2011) 932–936.
 - [87] J. Kim, S.-J. Lee, B.C. De Cooman, Effect of Al on the stacking fault energy of Fe–18Mn–0.6C twinning-induced plasticity, *Scr. Mater.* 65 (4) (2011) 363–366.
 - [88] Q.Z. Chen, B.J. Duggan, On cells and microbands formed in an interstitial-free steel during cold rolling at low to medium reductions, *Metall. Mater. Trans. A Phys. Metall. Mater. Sci.* 35A (11) (2004) 3423–3430.
 - [89] S. Mader, A. Seeger, H.-M. Thieringer, Work hardening and dislocation arrangement of fcc single crystals. II. Electron microscope transmission studies of Ni[single bond]Co single crystals and relation to work-hardening theory, *J. Appl. Phys.* 34 (11) (1963) 3376.
 - [90] A. Seeger, et al., Work-hardening and work-softening of face-centred cubic metal crystals, *Philos. Mag.* 2 (15) (1957) 323–350.
 - [91] H. Fujita, S. Kimura, Role of conjugate slip in deformation of Cu–10at.%Al single crystals, *J. Phys. Soc. Jpn.* 52 (1) (1983) 157–167.
 - [92] M.C. Ha, et al., Tensile deformation of a low density Fe–27Mn–12Al–0.8C duplex steel in association with ordered phases at ambient temperature, *Mater. Sci. Eng. A* 586 (0) (2013) 276–283.
 - [93] J. Fisher, E. Hart, R. Pry, Theory of Slip-band formation, *Phys. Rev.* 87 (6) (1952) 958–961.
 - [94] F. Pettinari, et al., Stacking fault energy in short-range ordered γ -phases of Ni-based superalloys, *Mater. Sci. Eng. A* 325 (1–2) (2002) 511–519.
 - [95] P. Müllner, et al., On the effect of nitrogen on the dislocation structure of austenitic stainless steel, *Mater. Sci. Eng. A* 164 (1–2) (1993) 164–169.
 - [96] P.M. Hazzledine, The mobility of dislocation groups, *Philos. Mag.* 18 (155) (1968) 1033–1039.
 - [97] P.M. Hazzledine, Work hardening in easy glide, *Can. J. Phys.* 45 (2) (1967) 765–775.
 - [98] P.M. Hazzledine, Dislocation multipoles, *Le Journal de Physique Colloques* 27 (C3) (1966) C3-210–C3-218.
 - [99] J.R. Low Jr., R.W. Guard, The dislocation structure of slip bands in iron, *Acta Metall.* 7 (3) (1959) 171–179.
 - [100] D.J. Bacon, U.F. Kocks, R.O. Scattergood, The effect of dislocation self-

- interaction on the Orowan stress, *Philos. Mag.* 28 (6) (1973) 1241–1263.
- [101] E. Demir, D. Raabe, F. Roters, The mechanical size effect as a mean-field breakdown phenomenon: example of microscale single crystal beam bending, *Acta Mater.* 58 (5) (2010) 1876–1886.
- [102] R. Rahimi, et al., Influence of Al on the temperature dependence of strain hardening behavior and glide planarity in Fe–Cr–Ni–Mn–C austenitic stainless steels, *Mater. Sci. Eng. A* 649 (2016) 301–312.
- [103] M.J. Marcinkowski, H. Chessin, Relationship between flow stress and atomic order in the FeCo alloy, *Philos. Mag.* 10 (107) (1964) 837–859.